Sustainable Energy & Fuels

Accepted Manuscript

This article can be cited before page numbers have been issued, to do this please use: W. Ma, X. Wu, K. Huang, M. Wang, R. Fu, H. Chen and S. Feng, *Sustainable Energy Fuels*, 2019, DOI: 10.1039/C9SE00337A.

ROYAL SOCIETY OF CHEMISTRY

rsc.li/sustainable-energy

View Article Online
DOI: 10.1039/C9SE00337A

Journal Name

ARTICLE

$Co(OH)_x$ nanolayer integrated planar WO_3/Fe_2O_3 photoanode for efficient photoelectrochemical water splitting

Received 00th January 20xx,
Accepted 00th January 20xx

DOI: 10.1039/x0xx00000x

www.rsc.org/

Wei Ma, Xiaofeng Wu, Keke Huang, Meng Wang, Rong Fu, Huanwen Chen and Shouhua Feng*

Hematite (a-Fe_2O_3), with a suitable bandgap of 2.2 eV, is an ideal photoanode material to convert solar light into hydrogen fuel via photoelectrochemical (PEC) water splitting. However, poor charge separation efficiency in the bulk and slow oxygen evolution kinetics at the Fe_2O_3/electrolyte interface have restricted its PEC performance to date. Here, we designed and fabricated a nanostructured WO_3/Fe_2O_3 thin film photoanode by electrospray technique to promote bulk charge separation of Fe_2O_3. An $Co(OH)_x$ nanolayer was further coated onto the surface by a solution-based chemisorption method to improve its oxygen evolution kinetics. We found the deposition amount ratio of WO_3 versus Fe_2O_3 and substrate temperature greatly influenced the PEC performance of WO_3/Fe_2O_3 photoanode. With optimal deposition amount ratio of 1:1 and substrate temperature of 400 °C, the WO_3/Fe_2O_3 photoanode shows a photocurrent of 0.32 mA cm^{-2} at 1.23 V_{RHE} which is more than 30-times higher than pure Fe_2O_3 film. Its photocurrent is further increased to 0.62 mA cm^{-2} after modified with $Co(OH)_x$ nanolayer and an obvious cathodic onset potential shift by about 160 mV is observed. The results show that this enhanced photoactivity is attributed to simultaneously improved charge carriers separation efficiency at the WO_3/Fe_2O_3 heterojunction interface and accelerated oxygen evolution kinetics at the surface.

Introduction

With ever increasing energy demand and growing environmental pollution, it is urgent to develop new energy storage and conversion technologies.[1, 2] Photoelectrochemical water splitting, which can convert solar energy to chemical energy of hydrogen by semiconductors like TiO_2, $BiVO_4$, α-Fe_2O_3 etc., offers a promising way to resolve these issues. However, the solar-to-hydrogen (STH) conversion efficiency is far below its theoretical value due to the oxygen evolution reaction limitation at the photoanodes, which is a four-electron process and kinetically sluggish.[3, 4] among these photoanodes, hematite (α-Fe_2O_3) is one of the most promising candidates for PEC water splitting owing to its favourable band gap energy (1.9-2.2eV), earth abundant, low cost and high stability in neutral and alkaline electrolyte.[5, 6] However, there are still several drawbacks leading to its practical performance far below its theoretically maximum (12.6 mA cm^{-2} under AM 1.5G), such as the low light absorption efficiency, poor electrical conductivity and charge separation efficiency, short hole transport distance (2–4 nm) and sluggish oxygen evolution reaction (OER) kinetics.[7, 8]

To address these issues, many strategies have been adopted including doping[9, 10], surface/interface passivation[11, 12] or cocatalyst decoration[13-15], charge storage layer modification[16], nanostructuring[17], and morphology engineering[18, 19]. Although these methods have largely improved the performance of Fe_2O_3, it still remains a great challenge to meet the expectation for adequate application. Recent studies have revealed that combining two semiconductors into a homojunction/heterojunction can be more efficient compare to single semiconductor photoanodes.[20-22] WO_3/Fe_2O_3 heterojunction has shown great potential for highly efficient PEC water splitting.[23-26] As proved by Yuan Li and co-workers, a core-shell WO_3/a-Fe_2O_3 Heterojunction Arrays photoelectrodes expanded the spectral range of light absorption and promoted photogenerated electron–hole separation/transfer of WO_3.[26] In addition, a layer of oxygen evolution cocatalyst (OEC) on the surface of a photoanode can further enhance the photoelectrochemical water splitting performance by improving sluggish oxygen evolution kinetics.[27] For example, Jae Young Kim et al. demonstrated that an ultrathin (ca. 2 nm) amorphous FeOOH deposited on the surface of hematite nanostructure significantly improved the water oxidation performance.[28]

Herein, we promote the performance of Fe_2O_3 by combining it with WO_3 (which is also a popular photoanode with a band gap of 2.7 eV and possesses good charge transport properties.[29]) to form a heterojunction and coating it with $Co(OH)_x$ nanolayer to simultaneously improve charge separation efficiency and oxygen evolution reaction kinetics. The WO_3/Fe_2O_3 heterojunction was fabricated by electrospray technique. And by a subsequent solution-based chemisorption, an ultrathin $Co(OH)_x$ OEC layer was coated (Scheme 1). The as synthesized $WO_3/Fe_2O_3/Co(OH)_x$ heterojunction exhibited a photocurrent density of 0.62 mA cm^{-2} which is more than 60-times higher than that of Fe_2O_3 at 1.23 V_{RHE} under air mass 1.5G illumination. The experimental

[a] State Key Laboratory of Inorganic Synthesis and Preparative Chemistry, College of Chemistry, Jilin University, Changchun 130012, P.R. China.
E-mail: shfeng@jlu.edu.cn

Electronic Supplementary Information (ESI) available: [details of any supplementary information available should be included here]. See DOI: 10.1039/x0xx00000x

View Article Online
DOI: 10.1039/C9SE00337A

results indicate that the enhanced charge separation efficiency in the bulk and charge injection efficiency at the OEC/electrolyte are responsible for the largely improved PEC performance.

Experimental section

Fluorine-doped tin oxide (FTO) glass was sequentially sonicated in ethanol, acetone, ethanol and distilled water each for 15 min. All the samples were deposited by homemade equipment (Fig. S1) the same used elsewhere.[30] The applied high voltage was 10.0 kV. The distance between the tip of the needle and the substrate was fixed at 10.0 cm. The flow rate was maintained at 15 μL min^{-1}.

Preparation of WO_3, Fe_2O_3, and WO_3/Fe_2O_3 photoanodes. Briefly, for preparing bare WO_3 film, 600 μL ammonium paratungstate solution (water/methol) was deposited on FTO substrate by electrospray. After deposition, the film was annealed at 500 °C for 2 h to obtain crystalline WO_3. For preparing bare Fe_2O_3 film, 600 μL Iron (III) acetylacetonate ethanol solution was deposited on FTO substrate. And the film was annealed at 550 °C for 2 h to obtain crystalline Fe_2O_3. For preparing WO_3/Fe_2O_3 (1:1) heterojunction, 300 μL ammonium paratungstate solution (water/methol) was firstly deposited on FTO substrate. After deposition, the film was annealed at 500 °C for 2 h to obtain crystalline WO_3. Then 300 μL Iron (III) acetylacetonate ethanol solution was deposited on the abovementioned WO_3. Finally, the film was annealed at 550 °C for 2 h to obtain crystalline WO_3/Fe_2O_3 heterojunction. The various ratios of WO_3/Fe_2O_3 photoanodes were prepared by adjusting the deposition amount.

Synthesis of $WO_3/Fe_2O_3/Co(OH)_x$ photoanode. The ultrathin $Co(OH)_2$ overlayer was coated on WO_3/Fe_2O_3 heterojunction using a solution-based chemisorption method. In brief, the WO_3/Fe_2O_3 heterojunction was immersed in a 0.2 M $Co(NO)_3$ solution at 85 °C for 5 h. The obtained $WO_3/Fe_2O_3/Co(OH)_x$ was washed by distilled water and dried by an air gun for further use.

Characterization. X-ray diffraction spectra measurement was performed on a a Rigaku D/Max 2500 V/PC X-ray diffractometer with Cu-Kα radiation (λ= 1.5418 Å) at 50 kV and 200 mA in the angle range of 20° to 80° with a scan speed of 2°/min at room temperature. The morphology of the samples was characterized by Scanning Electron Microscope (SEM, Helios NanoLab 600i Dual Beam System from FEI Company). Nanostructure of the samples was acquired by High-resolution Transmission Electron Microscopy (HRTEM, FEI Tecnai G2 S-Twin F20). X-ray Photoelectron Spectrum (XPS) was analyzed with Thermo ESCALAB 250 spectrometer (San Jose, CA, USA). The transmission spectra measurements were carried out using a Shimadzu UV-3600 spectrophotometer.

PEC Measurements. PEC Measurements were obtained with a CHI 660E electrochemical workstation (CH instruments Inc., shanghai) in a three-electrode configuration using the samples as working electrode, a Pt mesh as the counter, and a Ag/AgCl (sat. KCl, $E^0_{Ag/AgCl}$ = 0.1976 V at 25 °C) as the reference electrode. The as-prepared samples were directly used as the working electrode without further treatment. All the samples were measured in 1.0 M NaOH (pH=13.6) electrolyte with an exposed area of about 0.2 cm^2 through a round hole with a diameter of 5 mm. The measured potential vs Ag/AgCl (sat. KCl) was converted to reversible hydrogen electrode (RHE) following the Nernst equation: $E_{RHE} = E_{Ag/AgCl} + 0.059\ pH + E^0_{Ag/AgCl}$. The light source was provided by a 450 W xenon lamp, and the light intensity was adjusted to 100 mW cm^{-2}. During the PEC measurements, the illumination was conducted from the top side. The current-potential curves were tested with a scan rate of 10 mV s^{-1}. Amperometric i–t curves were measured at a bias voltage of 1.23 V_{RHE}. The incident photon-to-current conversion efficiency (IPCE) spectras were measured using a simulated sunlight and cut filters ranging from 350 nm to 550 nm. And the IPCE values at each wavelength were calculated by the following equation:[31]

$$IPCE\ (\%) = (1240 \times I)/(P_{light} \times \lambda) \times 100\%$$

Where λ is the wavelength of the incident light, and I and P_{light} are the measured photocurrent density and irradiance at some specific wavelength. Mott–Schottky measurements were obtained in the dark at a frequency of 1 kHz and scan rate of 10 mV s^{-1} from -0.5 to 0.5 V *vs*. Ag/AgCl. The Mott–Schottky equation was used according to literature.[9]

$$N_d = (2/e_0\varepsilon\varepsilon_0)[d(1/C^2)/dV]^{-1}$$

where e_0 = 1.60 × 10^{-19} C is the electron charge, ε=80 is the dielectric constant of hematite, ε_0 = 8.85 × 10^{-14} F cm^{-1} is the vacuum permittivity, C is the capacitance of the space charge region, V is the electrode applied potential, and N_d is the donor concentration.

Electrochemical impedance spectroscopy (EIS) was carried out at 0.23 V *vs*. Ag/AgCl with with an AC voltage amplitude of 5 mV and a frequency range of 0.1 to 100 kHz.

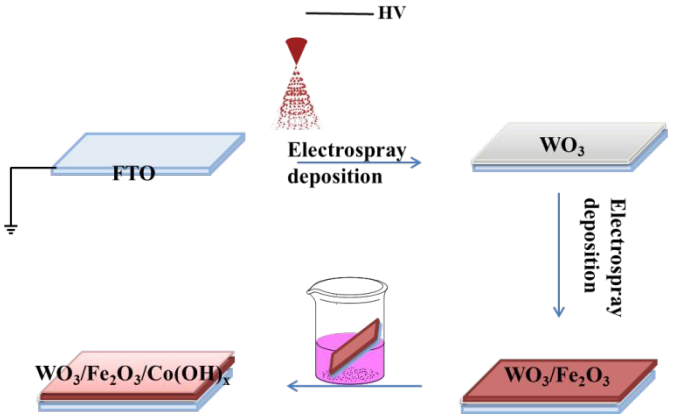

Scheme 1. Illustration of the preparation process of $WO_3/Fe_2O_3/Co(OH)_x$ photoanode.

Results and discussion

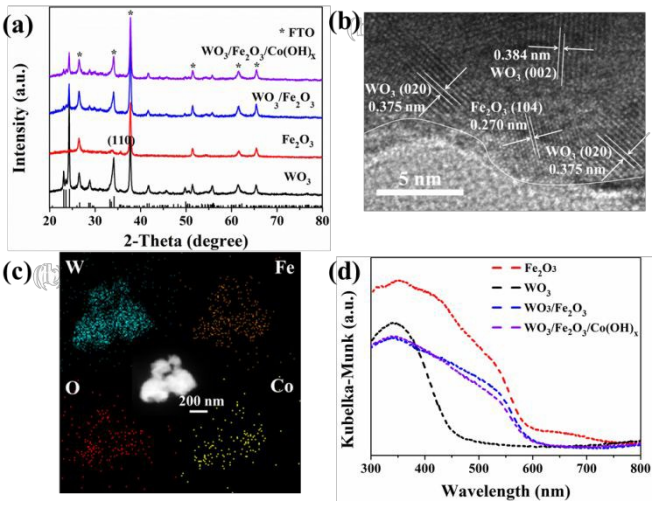

Figure 1. (a) XRD patterns of the samples, (b) HRTEM iamge and (c) EDS mapping of $WO_3/Fe_2O_3/Co(OH)_x$, (d) UV-Vis spectra of the samples.

Figure 1a shows the XRD patterns of Fe_2O_3 film, WO_3 film, WO_3/Fe_2O_3 heterojunction and $WO_3/Fe_2O_3/Co(OH)_x$ on FTO substrate. The crystalline structure of WO_3 is well indexed as monoclinic phase (JCPDS 83-0951). But it is hardly to obersve the XRD peaks of a-Fe_2O_3 except the (110) peak due to the low crystallization temperature. No obvious peaks corresponding to $Co(OH)_x$ were observed, possibly because of the small amount of $Co(OH)_x$ layer (probably less than 5%) and its amorphous nature. TEM is conducted to further characterize the structure of $WO_3/Fe_2O_3/Co(OH)_x$ as shown in Fig. 1b. The lattice spacing of 0.384 nm and 0.375 nm is well consisted with lattice spacing of the (002) planes and (020) planes of monoclinic WO_3. The lattice spacing of 0.270 nm is assigned to the (104) planes of hematite. The amorphous structure at the edge should be the amorphous $Co(OH)_x$ layer, which is about 2 nm thick. Figure 2c shows the EDS mapping image to conform the existence of this Co element. It can be seen after been treated, the surface of WO_3/Fe_2O_3 dose absorb certain amount of Co element and it is well distributed in the whole composite. The optical properties of the samples are measured by UV-Vis absorption spectra as shown in Fig. 1d. Notably, the absorption edge of pure WO_3 is at ca. 450 nm, which is in agreement with the band gap energy of 2.7eV as reported previously. The pure Fe_2O_3 shows an absorption onset below 600 nm with two absorption peaks at about 440 nm and 540 nm, which can be assigned to direct charge transfer and indirect transitions, respectively. The formation of WO_3/Fe_2O_3 heterojunction does not increase light absorption intensity or light absorption range compare to bare Fe_2O_3. The $WO_3/Fe_2O_3/Co(OH)_x$ shows nearly the same light absorption spectra as that of WO_3/Fe_2O_3 heterojunction.

We performed SEM characterization to confirm the morphology of the prepared photoanodes as shown in Figure 2. Pure Fe_2O_3 film is composed of dense and worm-like nanobars with a uniform size of tens of nanometer. Pure WO_3 film shows

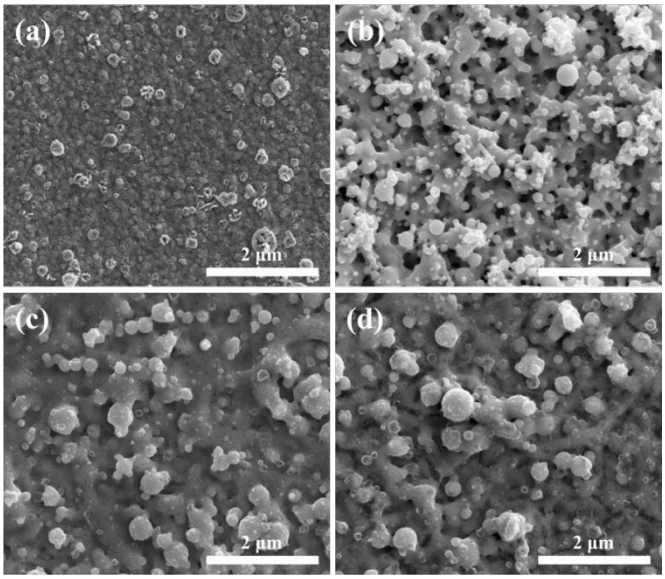

Figure 2. (a), (b), (c), and (d) show the SEM images of Fe_2O_3, WO_3, WO_3/Fe_2O_3, and $WO_3/Fe_2O_3/Co(OH)_x$, respectively.

irregular porous skeleton morphology. When Fe_2O_3 deposited on WO_3, it adopted a conformal deposition way using WO_3 as a growth skeleton. From Figure 2c we can clearly see that the morphology of WO_3/Fe_2O_3 is much like WO_3 except that the surface is coated by a layer of dense Fe_2O_3 nanoparticles. This uneven and porous surface structure may be beneficial for holes injection. And after depositing $Co(OH)_x$ layer, there is no obvious difference in morphology compare with WO_3/Fe_2O_3 heterojunction, indicating the conformal chemisorption growth. We also provided cross-section SEM images of the four samples as shown in Fig. S2. The pure Fe_2O_3 is densy and with a thickness of about 116 nm, while the WO_3 film was porous and much with a thickness 1.3 μm. This is due to part of Fe precursor is absobted on the electrospray device by electrostatic attraction. There is no significant difference between WO_3/Fe_2O_3, and $WO_3/Fe_2O_3/Co(OH)_x$, which are smooth at the top layer and keep characteristic of WO_3 at the down layer with a total thickness of about 180 nm.

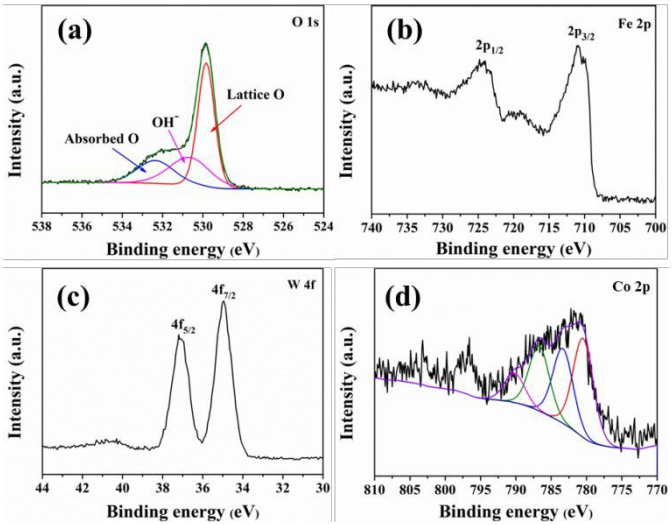

View Article Online
DOI: 10.1039/C9SE00337A

Figure 3. XPS spectra of O1s, Fe2p, W4f and Co2p of $WO_3/Fe_2O_3/Co(OH)_x$ respectively.

The surface properties of $WO_3/Fe_2O_3/Co(OH)_x$ are also investigated by XPS. Fig. 3a shows the fitting curve of O 1s spectra with three peaks at binding energies of 530.9, 531.9 and 529.9 eV, which account for lattice oxygen, oxygen in the $Co(OH)_x$ and surface adsorbed oxygen respectively. In Fig. 3b, there are two main peaks of Fe $2p_{1/2}$ and Fe $2p_{3/2}$ at 725.1 and 710.4 eV and a Fe $2p_{3/2}$ satellite peak at 719.3 eV, well consistent with the binding energy of Fe^{3+} in the α-Fe_2O_3 phase.[32] As shown in Fig. 3c the binding energies of W $4f_{5/2}$ at 37.2 eV and W $4f_{7/2}$ at 35.0 eV are in good agreement with the W^{6+} reported in the literature.[33] And the detected strong W 4f singal can be caused by the less conformal deposition of Fe_2O_3 nanoparticles. The Co 2p spectra has two main peaks at 797.0 and 780.8 eV (Fig. 3d), identical to the binding energies of Co $2p_{1/2}$ and Co $2p_{3/2}$, respectively. And the further fitting curves of Co $2p_{3/2}$ demonstrate the coexistence of Co^{2+} (783.2 eV) and Co^{3+} (780.4 eV) with their shake-up satellites (786.7 eV for Co^{2+} and 790.2 eV for Co^{3+}) in the $Co(OH)_x$.[34, 35] The valence state of Co species is also characterized after PEC water splitting (Figure S3). The Co 2p peaks shift to a higher binding energies after PEC water splitting, indicating the average valence state of Co species changes into a higher oxidized state.[36]

Fig. 4a shows the photocurrent-potential (I-V) curves of bare Fe_2O_3 film, bare WO_3 film, and WO_3/Fe_2O_3 heterojunction. The dark current densities are close to zero for all the samples from 0.8 to 1.8 V_{RHE}. Upon illumination, bare WO_3 film yields a photocurrent density of 0.13 mA cm^{-2}, while the bare Fe_2O_3 film shows a negligible photocurrent density of 0.01 mA cm^{-2} at 1.23 V_{RHE}, which may mainly due to its low crystallinity as shown in figure 1a. When the two materials form into WO_3/Fe_2O_3heterojunction, the photocurrent is greatly enhanced with a current density of 0.32 mA cm^{-2}. Since the WO_3/Fe_2O_3 heterojunction does not increase light absorption range compare to pure Fe_2O_3 film according to the UV-Vis spectrum, the significant enhanced photocurrent could not be explained by light absorption. It can be attributed to the improved charge separation efficiency at the WO_3/Fe_2O_3 heterojunction interface due to the inner built electric field due to the type II alignment. To see the effect of deposition amount ratio of WO_3 versus Fe_2O_3 on the PEC performance, WO_3/Fe_2O_3 heterojunction is optimised with different deposition amount ratios as shown in Fig. 4b. It reveals that the performance has a volcano relationship with the deposition amount ratio, reaching its optimized value at the ratio of 1:1. When the ratio is higher or lower, the activity begins to decline but still shows much higher value compare to bare WO_3 or Fe_2O_3 film. This may because too thick WO_3 is unfavourable for photogenerated electrons to transfer to the FTO substrate and too thick Fe_2O_3 leads to larger ohmic resistance and introduces more grain boundaries and interfaces as well which is unfavourable for charge separation and photogenerated holes diffusion.[37] The optimal WO_3/Fe_2O_3 heterojunction reached a photocurrent density of 0.32 mA cm^{-2} at 1.23 V_{RHE}, which is much higher than that of other ratios. Moreover, the saturated photocurrent density is also much higher than that of other ratios. Since the substrate temperature usually plays an important role in film deposition,[38] we adjusted the deposition temperature to get a proper one. It can be seen from LSV curves in Fig. 4c that the best substrate temperature for deposition is 400 °C. The photocurrent densities at 1.23 V_{RHE} are almost the same, but the saturated photocurrent densities of flat region are quite different. The photocurrent density in the flat region of the sample deposited at 400 °C is much higher than others. This can be attributed to the surface morphology difference deposited at different substrate temperature as shown in Figure S4. The film is dense and bulky at low substrate temperature, with elevated substrate temperature the surface is porous and composed nanoparticles. Further increases the substrate temperature, the particles begin to agglomerate to form large particles. This is because it is not helpful for desolvation process of electrospray at low substrate temperature, resulting in dense and bulky film. However, at high substrate temperature, nanoparticles can aggregate rapidly to form big particles. After modified with an ultrathin $Co(OH)_x$ layer, the photocurrent further increases to 0.62 mA cm^{-2} at V_{RHE}. The catalyst has no role on increasing the charge density assuming no absorption due to its very low thickness. Besides, the onset potential shifts toward cathode by about 160 mV compare to that of WO_3/Fe_2O_3 heterojunction (the potential at the intersection point of the dark current and the tangent at the maximum slope of the photocurrent is used to calculate the onset potential shift), indicating that the ultrathin $Co(OH)_x$ layer accelerates water oxidation kinetics.

The transient photocurrents were obtained at 1.23 V_{RHE} by intermittent irradiation. As shown in Fig. 5a, pure WO_3 shows unstable performance due to the dissolving of WO_3 in strong alkaline electrolyte. The photocurrent of WO_3/Fe_2O_3 photoanode slightly decreases over time. It is worth noting that the $WO_3/Fe_2O_3/Co(OH)_x$ exhibits a good stability without any decline during intermittent irradiation for 200 s. Long term stability of photoanodes was also examined (Figure S5). Both of WO_3/Fe_2O_3 and $WO_3/Fe_2O_3/Co(OH)_x$ display almost the same long term stability. The current density of WO_3/Fe_2O_3 increases in the beginning and then gradually declines. While $WO_3/Fe_2O_3/Co(OH)_x$ shows steady current density within 600 s and then starts to gradually decline. And the $Co(OH)_x$ increases

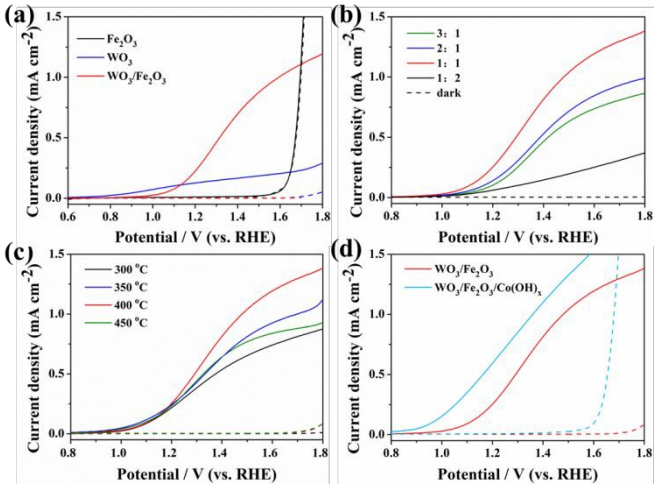

Figure 4. (a) LSV curves of the Fe_2O_3, WO_3, the WO_3/Fe_2O_3, (b) LSV curves of WO_3/Fe_2O_3 with different thickness ratio of WO_3:Fe_2O_3, (c) LSV curves of WO_3/Fe_2O_3 deposited at different substrate temperatures, and (d) LSV curves of WO_3/Fe_2O_3 and $WO_3/Fe_2O_3/Co(OH)_x$.

the short time stability but does not increase the long term stability of $WO_3/Fe_2O_3/Co(OH)_x$. IPCE values are presented in

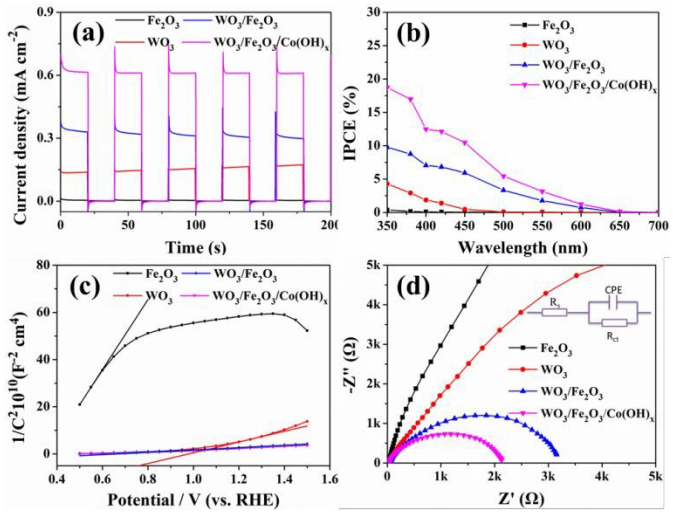

Figure 5. (a) Amperometric i-t curves taken at 1.23 V_{RHE} (b) IPCE spectra measured at 1.23 V_{RHE} (c) M-S plots collected at a frequency of 1 kHz in the dark from -0.5 to 0.5 $V_{Ag/AgCl}$ and (d) EIS spectra of Fe_2O_3, WO_3, WO_3/Fe_2O_3 and $WO_3/Fe_2O_3/Co(OH)_x$ photoanodes conducted at 1.23 V_{RHE}.

Fig. 5b, which are in good with the J-V curves (Fig. 3a and Fig. 3d). The IPCE values for bare WO_3 film and bare Fe_2O_3 film are almost zero in the visible light region. After formation of WO_3/Fe_2O_3 heterojunction, a remarkable enhancement of IPCE values can be obtained in the whole spectrum, suggesting WO_3/Fe_2O_3 heterojunction effectively improves the incident photon-to-current conversion efficiency compare to bare WO_3 film and bare Fe_2O_3 film. An ultrathin $Co(OH)_x$ layer on WO_3/Fe_2O_3 further boosts the IPCE values, reaching 19% at 350 nm which is over 50 times higher than that of bare Fe_2O_3 film. Besides, Motty-schottky plots (Fig. 5c) were obtained to investigate the carrier densities of the samples. The carrier densities calculated from the slopes of the Mott–Schottky plots for Fe_2O_3, WO_3, WO_3/Fe_2O_3 and $WO_3/Fe_2O_3/Co(OH)_x$ photoanodes are 1.2×10^{18} cm^{-3}, 7.7×10^{18} cm^{-3}, 3.6×10^{19} cm^{-3} and 3.9×10^{19} cm^{-3}, respectively. It obviously shows that after forming heterojunction with WO_3, the donor density increases more than one magnitude compare with bare Fe_2O_3, indicating that combine WO_3 to form heterojunction is an effective way to improve electrical conductivity and the charge transportation of Fe_2O_3. The modification of ultrathin $Co(OH)_x$ layer does not change the donor density of the WO_3/Fe_2O_3 heterojunction, demonstrating the improved performance of $WO_3/Fe_2O_3/Co(OH)_x$ photoanode compare to WO_3/Fe_2O_3 is owing to enhanced charge separation efficiency and the accelerated OER kinetics at the surface. To further elucidate charge separation as well as the charge transfer behaviour, EIS measurement was carried out for the photoanodes (Fig. 5d). The experimental data are fitted by using an equivalent circuit R_s (CPE-R_{ct}) and the values are presented in Table S1, in which R_s is the ohmic contribution, CPE is a constant phase element that takes into account non-idealities in the capacitance of the Helmholtz layer, and R_{ct} is the charge-transfer resistance.[39] The charge transfer process at the electrode/electrolyte interface can be reflected by the semicircle of the Nyquist plots. The smaller the low-frequency semicircle is, the faster the charge

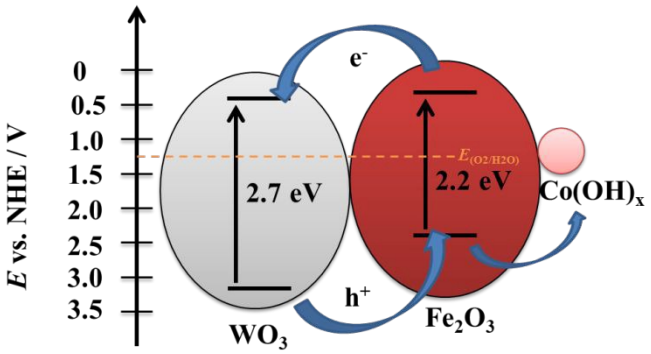

Figure 6. Schematic of the band diagram of the $WO_3/Fe_2O_3/Co(OH)_x$ heterojunction photoanode for photoelectrochemical water oxidation.

transfer of photogenerated carriers. It can be obviously seen from the fitted plots that WO_3/Fe_2O_3 heterojuction possess a relatively smaller diameter of the curve compare to that of bare Fe_2O_3 and bare WO_3, which means much faster charge transfer kinetics at the electrode interface. The ultrathin $Co(OH)_x$ layer modified WO_3/Fe_2O_3 shows the smallest resistance, which is consistent with the performance of the samples. These results further indicate WO_3/Fe_2O_3 heterojunction can significantly reduce the charge transfer resistance to improve the charge separation efficiency in the bulk, while the ultrathin $Co(OH)_x$ layer can enhance the charge separation at the electrode/electrolyte interface.

All the aforementioned results indicates that the planar $WO_3/Fe_2O_3/Co(OH)_x$ photoanode exhibites improved activity for photoelectrochemical water oxidation (Figure 6). Due to the suitable band diagram of WO_3 and Fe_2O_3, it can form an inner built electric field at the WO_3/Fe_2O_3 interface. Under illumination, the photogenerated holes can spontaneously inject into the valence Fe_2O_3 from the valence band of WO_3 and migrate to the surface to oxidize water, while the photogenerated electrons of Fe_2O_3 migrate to FTO substrate through the conduction band of WO_3.[25] The $Co(OH)_x$ nanolayer, which acts as an hole tranport layer, can efficiently collect photogenerated holes and then generate active Co^{4+} species to oxidate water. After oxidating water, the Co^{4+} species will be reduced to their original valence state to capture holes. Thus, the $Co(OH)_x$ not only accelerates oxygen evolution kinetics but also protects WO_3/Fe_2O_3 photoanode from photocorrosion by the holes accumulation.

Conclusions

In summary, a planar WO_3/Fe_2O_3 heterojunction film was constructed by electrospray technique for PEC water splitting. And an $Co(OH)_x$ surface nanolayer was introduced to further improve the performance of the heterojunction. This $WO_3/Fe_2O_3/Co(OH)_x$ photoanode exhibited a significant improvement in water oxidation which is more than 30 times higher than that of pure Fe_2O_3 and nearly 2 times of that of WO_3/Fe_2O_3 heterojunction at 1.23V vs RHE in 1 $_M$ NaOH solution under air mass 1.5G illumination (100 mW cm^{-2}). Moreover, an obvious cathodic shift by about 160 mV on the

onset potential was observed after $Co(OH)_x$ modification. This remarkable enhancement of PEC performance was attributed to the improved charge separation at the WO_3/Fe_2O_3 interface and the accelerated water oxidation kinetics at the surface of the photoanode. This strategy by simultaneously enhancing charge separation efficiency in the bulk and accelerating oxygen evolution kinetics at the electrode/electrolyte interface offers a promising way to design highly efficient photoanodes.

Conflicts of interest

There are no conflicts to declare.

Acknowledgements

This work was supported by National Nature Science Foundation of China (grants 21427802, 21671076 and 21621001).

Notes and references

1. R. Liu, Z. Zheng, J. Spurgeon and X. Yang, *Energy Environ. Sci.*, 2014, **7**, 2504-2517.
2. H. Wang, L. Zhang, Z. Chen, J. Hu, S. Li, Z. Wang, J. Liu and X. Wang, *Chem. Soc. Rev.*, 2014, **43**, 5234-5244.
3. Y. Park, K. J. McDonald and K. S. Choi, *Chem. Soc. Rev.*, 2013, **42**, 2321-2337.
4. M. W. Kanan and D. G. Nocera, *Science*, 2008, **321**, 1072-1075.
5. D. Cao, W. Luo, J. Feng, X. Zhao, Z. Li and Z. Zou, *Energy Environ. Sci.*, 2014, **7**, 752-759.
6. L. Wang, K. Marcus, X. Huang, Z. Shen, Y. Yang and Y. Bi, *Small*, 2018, **14**, e1704464.
7. H. Dotan, O. Kfir, E. Sharlin, O. Blank, M. Gross, I. Dumchin, G. Ankonina and A. Rothschild, *Nat. Mater.*, 2013, **12**, 158-164.
8. J. Li, S. K. Cushing, P. Zheng, F. Meng, D. Chu and N. Wu, *Nat. Commun.*, 2013, **4**, 2651.
9. Z. Luo, C. Li, S. Liu, T. Wang and J. Gong, *Chem. Sci.*, 2017, **8**, 91-100.
10. J. Liu, Y. Y. Cai, Z. F. Tian, G. S. Ruan, Y. X. Ye, C. H. Liang and G. S. Shao, *Nano Energy*, 2014, **9**, 282-290.
11. H. Lan, A. Wei, H. Zheng, X. Sun and J. Zhong, *Nanoscale*, 2018, **10**, 7033-7039.
12. X. Yang, R. Liu, Y. Lei, P. Li, K. Wang, Z. Zheng and D. Wang, *ACS Appl. Mater. Interfaces.*, 2016, **8**, 16476-16485.
13. F. Malara, A. Minguzzi, M. Marelli, S. Morandi, R. Psaro, V. Dal Santo and A. Naldoni, *ACS Catalysis*, 2015, **5**, 5292-5300.
14. X. Long, F. Li, L. Gao, Y. Hu, H. Hu, J. Jin and J. Ma, *ChemSusChem*, 2018, **11**, 4094-4101.
15. F. Li , J. Li , L. Gao , Y. Hu , X. Long , S. Wei , C. Wang , J. Jin, J. Ma, *J. Mater. Chem. A,* 2018, **6**, 23478-23485.
16. L. Li, X. Yang, Y. Lei, H. Yu, Z. Yang, Z. Zheng and D. Wang, *Chemical Science*, 2018, **9**, 8860-8870.
17. A. Kay, I. Cesar and M. Grätzel, *J. Am. Chem. Soc.,* 2006, **128**, 15714-15721.
18. M. Li, Y. Yang, Y. Ling, W. Qiu, F. Wang, T. Liu, Y. Song, X. Liu, P. Fang, Y. Tong and Y. Li, *Nano Lett.*, 2017, **17**, 2490-2495.
19. H. S. Han, S. Shin, D. H. Kim, I. J. Park, J. S. Kim, P.-S. Huang, J.-K. Lee, I. S. Cho and X. Zheng, *Energy Environ. Sci.*, 2018, **11**, 1299-1306.
20. S. J. Hong, S. Lee, J. S. Jang and J. S. Lee, *Energy Environ. Sci.*, 2011, **4**, 1781.
21. S. Shen, S. A. Lindley, X. Chen and J. Z. Zhang, *Energy Environ. Sci.*, 2016, **9**, 2744-2775.
22. F. Li, J. Li, F. Li, L. Gao, X. Long, Y. Hu, C. Wang, S. Wei, J. Jin and J. Ma, *J. Mater. Chem. A,* 2018, **6**, 13412-13418.
23. K. H. Ng, L. J. Minggu, W. F. Mark-Lee, K. Arifin, M. H. H. Jumali and M. B. Kassim, *Mater. Res. Bull.*, 2018, **98**, 47-52.
24. X. Fan, T. Wang, H. Xue, B. Gao, S. Zhang, H. Gong, H. Guo, L. Song, W. Xia and J. He, *ChemElectroChem*, 2019, **6**, 543-551.
25. T. Jin, P. Diao, Q. Wu, D. Xu, D. Hu, Y. Xie and M. Zhang, *Appl. Catal., B*, 2014, **148-149**, 304-310.
26. Y. Li, L. Zhang, R. Liu, Z. Cao, X. Sun, X. Liu and J. Luo, *ChemCatChem*, 2016, **8**, 2765-2770.
27. T. W. Kim and K.-S. Choi, *Science*, 2014. **343**, 990.
28. J. Y. Kim, D. H. Youn, K. Kang and J. S. Lee, *Angew. Chem., Int. Ed.,* 2016, **55**, 10854-10858.
29. J. Zhang, X. Chang, C. Li, A. Li, S. Liu, T. Wang and J. Gong, *J. Mater. Chem. A*, 2018, **6**, 3350-3354.
30. M. Wang, X. Wu, K. Huang, Y. Sun, Y. Zhang, H. Zhang, J. He, H. Chen, J. Ding and S. Feng, *Nanoscale*, 2018, **10**, 6678-6683.
31. Q. Rui, L. Wang, Y. Zhang, C. Feng, B. Zhang, S. Fu, H. Guo, H. Hu and Y. Bi, *J. Mater. Chem. A*, 2018, **6**, 7021-7026.
32. F. Li, J. Li, J. Zhang, L. Gao, X. Long, Y. Hu, S. Li, J. Jin and J. Ma, *ChemSusChem*, 2018, **11**, 2156-2164.
33. A. J. E. Rettie, K. C. Klavetter, J.-F. Lin, A. Dolocan, H. Celio, A. Ishiekwene, H. L. Bolton, K. N. Pearson, N. T. Hahn and C. B. Mullins, *Chem. Mater.*, 2014, **26**, 1670-1677.
34. H. L. Jing Yang, Wayde N. Martens, and Ray L. Frost, *J. Phys. Chem. C*, 2010, **114**, 111–119.
35. G. Dong, H. Hu, L. Wang, Y. Zhang and Y. Bi, *J. Catal.*, 2018, **366**, 258-265.
36. S. Li, Q. Zhao, D. Meng, D. Wang and T. Xie, *J. Mater. Chem. A*, 2016, **4**, 16661-16669.
37. Y.-F. Lin and Y.-J. Hsu, *Appl. Catal., B*, 2013, **130-131**, 93-98.
38. G. Rahman and O.-S. Joo, *J. Mater. Chem. A,* 2013, **1**, 5554.
39. L. Gao, F. Li, H. Hu, X. Long, N. Xu, Y. Hu, S. Wei, C. Wang, J. Ma and J. Jin, *ChemSusChem*, 2018, **11**, 2502-2509.

View Article Online
DOI: 10.1039/C9SE00337A

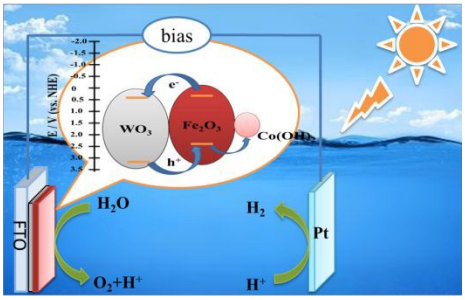

$Co(OH)_x$ integrated composition controllable planar Fe_2O_3/WO_3 photoanode prepared by electrospray technique for enhanced PEC performance.